Polar Topographic Derivatives for 3D Face Recognition: Application to Internet of Things Security

Farshid Hajati[1(✉)], Ali Cheraghian[2], Omid Ameri Sianaki[1], Behnam Zeinali[3], and Soheila Gheisari[4]

[1] College of Engineering and Science, Victoria University Sydney, Sydney, Australia
{farshid.hajati,omid.amerisianaki}@vu.edu.au
[2] College of Engineering and Computer Science,
The Australian National University, Canberra, Australia
u5942646@anu.edu.au
[3] Electrical Engineering Department,
Iran University of Science and Technology, Tehran, Iran
zeinali.behnam@gmail.com
[4] Faculty of Engineering and Information Technology,
University of Technology Sydney, Ultimo, Australia
soheila.gheisari@student.uts.edu.au

Abstract. We propose Polar Topographic Derivatives (PTD) to fuse the shape and texture information of a facial surface for 3D face recognition. Polar Average Absolute Deviations (PAADs) of the Gabor topography maps are extracted as features. High-order polar derivative patterns are obtained by encoding texture variations in a polar neighborhood. By using the and Bosphorus 3D face database, our method shows that it is robust to expression and pose variations comparing to existing state-of-the-art benchmark approaches.

1 Introduction

Automatic face recognition has many commercial, military and security applications such as Internet of Things (IoT) [1,2]. Despite the significant progress in face recognition technology, recognizing a face under the unconstrained condition is still challenging. There are five major challenging problems in face recognition which are changing the illumination condition, facial expressions, head pose variations, occlusions, and aging [3]. Many of the face recognition algorithms are categorized as holistic which use the whole face image for feature extraction. Alyuz et al. [7] constructed seven meaningful regions: the nose, the left/right eye, the forehead, the left/right cheek, and the mouth-chin. By partitioning the 3D face image into different paths their scheme was fast and accurate. To heighten the accuracy, the results were fused in decision level after applying the Linear Discriminate Analysis (LDA) to patches. Smeets et al. [6] proposed a local feature method for 3D face, called meshSIFT in which important points are

detected as extrema in a scale space then a canonical orientation is assigned to those points based on the surface normals in the scale-dependent local neighborhood. Concatenated histograms of slant angles and shape indices is described as a feature vector. In Recent methods in the face recognition have used both the texture (2D) and the shape (3D) information to improve the performance. Bowyer et al. research [5] the fact that multimodal face recognition systems have better accuracy compared to the shape and the texture-based face recognition algorithms was investigated. Chang et al. [4] showed a new method by applying a PCA-based algorithm to the both texture and shape of face image and fusing the matching scores. Using a gallery of 275 subjects, a recognition rate of 93% and 99% for 3D and multimodal face recognition was reported respectively. Malassiotis and Strintzis [10] shows a method to overcome pose variations in the corresponding texture map by using the range map. In Bronstein et al. research [11], by finding an isometric-invariant representation of the face, the effects of expressions were removed and new expression-invariant multimodal face recognition algorithm was proposed.

In Mian et al. [12] proposed method, in order to achieve efficiency and robustness to facial expressions, a fully automatic multimodal face recognition algorithm and performs hybrid (feature based and holistic) matching was used. The novel 3D Spherical Face Representation (SFR) and Scale-Invariant Feature Transform (SIFT) descriptor were used to form a rejection classifier and the results of all matching engines were fused at the metric level to achieve higher accuracy. Hajati et al. [8] proposed new algorithm in which expression and pose invariant 3D face recognition features were extracted by using Patch Geodesic Distance (PGD). In PGD, 3D face images are partitioned into equal-sized square patches in a non-overlapping manner. To encode the shape adjusted textures into patterns, Local geodesic paths within patches and global geodesic paths for patches are combined.

2   Polar Topographic Derivatives (PTD)

The topography map is one of the most important shape representation methods in 3D space. A topography map shows the physical features of a surface and their structural relationships. A topography map reveals the relief of a surface by means of level curves (contour lines). Lines that joint equal-height points on the surface above or below a reference point is known as a Level curves. The highest point in the topography map usually known as a reference point. Figure 1 indicates an example of level curves in a face surface and the corresponding topography map.

Imagine a surface $z(x, y)$, the level curve with the height index h, L^h, is obtained by

$$L^h = \{z(x,y) | z_{\max} - hw_z < z(x,y) < z_{\max} - (h-1)w_z\};$$
$$h = 1, 2, ..., \lfloor z_{\max}/w_z \rfloor + 1 \tag{1}$$

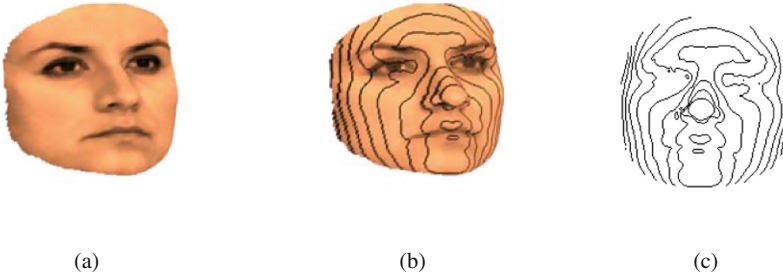(a)   (b)   (c)

Fig. 1. Level curves and topography map. (a) original 3D face surface, (b) surface level curves, (c) topography map

where z_{max} is the maximum height (reference) point in the surface, w_z is the step size of the level curve, h is the height index of the level curve, and $\lfloor \cdot \rfloor$ denotes the floor function.

Given the level curves ℓ^h, the topography map $T(x, y)$ is indicated as

$$T(x, y) = \begin{cases} 1, & if \quad (x, y, z) \in \ell^h \\ 0, & if \quad (x, y, z) \notin \ell^h \end{cases} \tag{2}$$

After extracting the topography map from the face surface, Gabor wavelet is applied to the topography map. The Gabor wavelets are represented as follows [9]:

$$\varphi_{\mu,v}(z) = \frac{k_{\mu,v}^2}{\sigma^2} \exp\left(-\frac{k_{\mu,v}^2 z^2}{2\sigma^2}\right)[\exp(ik_{\mu,v}) - \exp(-\frac{\sigma^2}{2})] \tag{3}$$

where μ and v denote the orientation and the scale of the Gabor wavelets, respectively. In Eq. (3), $k_{\mu,v}$ is defined as

$$k_{\mu,v} = k_v e^{i\varphi_\mu} \tag{4}$$

where $k_v = k_{max}/f^v$ and $\varphi_\mu = \pi\mu/8$. k_{max} is the maximum frequency, and f is the spacing factor between kernels in the frequency domain. We use Gabor kernels with five different scales, $v \in \{0, ..., 4\}$, and eight orientations, $\mu \in \{0, ..., 7\}$, with the parameters $\sigma = 2\pi$, $k_{max} = \pi/2$, and $f = \sqrt{2}$.

Polar Gabor topography maps are the convolution of the topography map with the Gabor kernels in the polar coordinates as

$$PGT_{\mu,v}(r, \theta) = T(x, y) * \varphi_{\mu,v}(z) \tag{5}$$

$$r = \sqrt{(x - x_{rp})^2 + (y - y_{rp})^2} \tag{6}$$

$$\theta = \begin{cases} 0, & if\ x = x_{rp},\ y = y_{rp} \\ \tan^{-1}(\frac{y-y_{rp}}{x-x_{rp}}), & if\ x \geq x_{rp} \\ \tan^{-1}(\frac{y-y_{rp}}{x-x_{rp}}) + \pi, & if\ x < x_{rp} \end{cases} \tag{7}$$

where x_{rp} and y_{rp} are the coordinates of the reference point (nose tip). Polar Gabor topography maps are divided into non-overlapping polar patches. Here, we label the patch points with p and q indexes as

$$p = \lfloor r/w_r \rfloor + 1;\ \ 0 \leq r < r_{max} \tag{8}$$

$$q = \lfloor \theta/w_\theta \rfloor + 1;\ \ 0 \leq \theta < 2\pi \tag{9}$$

the patch sizes in the radial and the angular directions are shown by w_r and w_θ respectively, and indicate as

$$w_r = r_{max}/N_r \tag{10}$$

$$w_\theta = 2\pi/3(2p-1) \tag{11}$$

where r_{max} and N_r indicate the maximum radius and the number of sectors in the radial direction, respectively.

In the proposed polar patching, the total amount of patches, N_p, is

$$N_p = \sum_{k=1}^{\lfloor r_{\max}/w_r \rfloor} 3(2k-1) \tag{12}$$

The (p,q)th patch of the Gabor topography map, $GT_{pq}(r^{pq}, \theta^{pq})$, is represented as

$$PGT_{\mu,v}^{pq}(r^{pq}, \theta^{pq}) = PGT_{\mu,v}(w_r\,(p-1) + r^{pq}, w_\theta\,(q-1) + \theta^{pq}) \tag{13}$$

where r^{pq} and θ^{pq} are the coordinates of the (p,q)th patch. For each patch, we compute Polar Average Absolute Deviation (PAADs) from the mean of the patch's gray levels. For the (p,q)th patch of the polar Gabor topography map, the PAAD feature from the mean of the gray levels is defined as

$$PAAD_{\mu,v}^{pq} = \frac{1}{N}\left(\sum_{r^{pq}}\sum_{\theta^{pq}}\left|PGT_{\mu,v}^{pq}\,(r^{pq}, \theta^{pq}) - \overline{PGT_{\mu,v}^{pq}\,(r^{pq}, \theta^{pq})}\right|\right) \tag{14}$$

where $PGT_{\mu,v}^{pq}\,(r^{pq}, \theta^{pq})$ is the (p,q)th patch of the Polar Gabor topography map. N is the number of pixels in the (p,q)th patch and $\overline{PGT_{\mu,v}^{pq}\,(r^{pq}, \theta^{pq})}$ is the mean of the (p,q)th patch's gray levels.

By concatenating the PAADs of (p,q)th patch in different scales and orientations, we obtain a new feature vector, called Polar Gabor Topography Vector (PGTV), as

$$PGTV^{pq} = \{PAAD_{\mu,v}^{pq}|\mu = 0,\ldots,7\ \&\ v = 0,\ldots,4\} \tag{15}$$

where $PAAD_{\mu,v}^{pq}$ is computed using the μ and v as the scale and the orientation. We also use high-order polar information in the texture map of the object to extract discriminant features. First, we transform the texture map into the polar coordinates. Given a texture map, $f(x, y)$, the transformed texture map in the polar coordinates, $F(r, \theta)$, is defined as

$$F(r, \theta) = f(x, y) \tag{16}$$

where r and θ are computed using Eqs. (6) and (7).

We partitioned the texture map into predefined patches and extracted derivatives within patches to compute local features. We partitioned the texture map into non-overlapping polar patches using Eqs. (8)-(11) as

$$F^{pq}\left(r^{pq}, \theta^{pq}\right) = F(w_r\left(p-1\right) + r^{pq}, w_\theta\left(q-1\right) + \theta^{pq}) \tag{17}$$

where r^{pq} and θ^{pq} are the coordinates of the (p, q)th patch of the partitioned texture map.

Let $F^{pq}(r_0^{pq}, \theta_0^{pq})$ be a point of the (p, q)th patch of the texture map, the eight neighbors of the point are defined as

$$F^{pq}(r_i^{pq}, \theta_j^{pq}) = F^{pq}(r^{pq} + i.\Delta r, \theta^{pq} + j.\Delta\theta) \; ; \; i, j = -1, 0, 1 \; \& \; i = j \neq 0 \tag{18}$$

where Δr and $\Delta\theta$ are the radial and the angular resolutions of the texture map. Here, we assume $\Delta\theta = \pi \cdot \Delta r/180$.

The angular directions with different orders and the derivative along the radial can be computed after determining the 8-neighborhood of the point $F^{pq}(r_0^{pq}, \theta_0^{pq})$. The first-order polar derivatives along the radial and the angular directions of $F^{pq}(r_0^{pq}, \theta_0^{pq})$ are defined as

$$\partial F^{pq}\left(r_0^{pq}, \theta_0^{pq}\right)/\partial r = F^{pq}(r_0^{pq}, \theta_0^{pq}) - F^{pq}(r_1^{pq}, \theta_0^{pq}) \tag{19}$$

$$\partial F^{pq}\left(r_0^{pq}, \theta_0^{pq}\right)/\partial\theta = F^{pq}(r_0^{pq}, \theta_0^{pq}) - F^{pq}(r_0^{pq}, \theta_1^{pq}) \tag{20}$$

Similarly, the second-order polar derivatives are defined as

$$\partial^2 F^{pq}\left(r_0^{pq}, \theta_0^{pq}\right)/\partial r^2 = \partial F^{pq}\left(r_0^{pq}, \theta_0^{pq}\right)/\partial r - \partial F^{pq}(r_1^{pq}, \theta_0^{pq})/\partial r \tag{21}$$

$$\partial^2 F^{pq}\left(r_0^{pq}, \theta_0^{pq}\right)/\partial\theta^2 = \partial F^{pq}\left(r_0^{pq}, \theta_0^{pq}\right)/\partial\theta - \partial F^{pq}(r_0^{pq}, \theta_1^{pq})/\partial\theta \tag{22}$$

Generally, the nth-order polar derivatives are defined using the $(n-1)^{th}$-order polar derivatives as

$$\partial^{(n)} F^{pq}\left(r_0^{pq}, \theta_0^{pq}\right)/\partial r^{(n)} =$$
$$\partial^{(n-1)} F^{pq}\left(r_0^{pq}, \theta_0^{pq}\right)/\partial r^{(n-1)} - \partial^{(n-1)} F^{pq}(r_1^{pq}, \theta_0^{pq})/\partial r^{(n-1)} \tag{23}$$

$$\partial^{(n)} F^{pq}\left(r_0^{pq}, \theta_0^{pq}\right)/\partial\theta^{(n)} =$$
$$\partial^{(n-1)} F^{pq}\left(r_0^{pq}, \theta_0^{pq}\right)/\partial\theta^{(n-1)} - \partial^{(n-1)} F^{pq}(r_0^{pq}, \theta_1^{pq})/\partial\theta^{(n-1)} \tag{24}$$

By using the unit step function, the computed derivatives are encoded into binary bits, there for binary patterns called Polar Derivative Patterns (PDP) are formed. The nth-order Polar Derivative Patterns (PDP) along the radial direction, $PDP_r(F^{pq}(r_0^{pq}, \theta_0^{pq}))$, and along the angular direction, $PDP_\theta(F^{pq}(r_0^{pq}, \theta_0^{pq}))$, in the (p,q)th patch are defined as

$$
\begin{aligned}
PDP_r^{pq}\left(F^{pq}\left(r_0^{pq}, \theta_0^{pq}\right)\right) = \\
2^0.u\left(\partial^{(n)}F^{pq}(r_0^{pq}, \theta_0^{pq})/\partial r^{(n)} \cdot \partial^{(n)}F^{pq}(r_1^{pq}, \theta_1^{pq})/\partial r^{(n)}\right) + \cdots \\
+2^7.u\left(\partial^{(n)}F^{pq}(r_0^{pq}, \theta_0^{pq})/\partial r^{(n)} \cdot \partial^{(n)}F^{pq}(r_0^{pq}, \theta_1^{pq})/\partial r^{(n)}\right)
\end{aligned}
\tag{25}
$$

$$
\begin{aligned}
PDP_\theta^{pq}\left(F^{pq}\left(r_0^{pq}, \theta_0^{pq}\right)\right) = \\
2^0.u\left(\partial^{(n)}F^{pq}(r_0^{pq}, \theta_0^{pq})/\partial \theta^{(n)} \cdot \partial^{(n)}F^{pq}(r_1^{pq}, \theta_1^{pq})/\partial \theta^{(n)}\right) + \cdots \\
+2^7.u\left(\partial^{(n)}F^{pq}(r_0^{pq}, \theta_0^{pq})/\partial \theta^{(n)} \cdot \partial^{(n)}F^{pq}(r_0^{pq}, \theta_1^{pq})/\partial \theta^{(n)}\right)
\end{aligned}
\tag{26}
$$

where $u(\cdot)$ is the unit step function determines the direction of the derivatives transition.

It can be easily observed that by increasing the operator order from the first-order to the second-order, the third-order, and up to the fourth-order, finer details are extracted from the face surface. It is also evident that in higher order patterns, e.g. fourth-order, more noise comes into the features rather than identity information.

Eventually, by concatenating the spatial histogram to make a feature vector as the distribution of the PDPs is modeled:

$$
HPDP^{pq} = \{HPDP_r^{pq}, HPDP_\theta^{pq}\}
\tag{27}
$$

where $HPDP_r^{pq}$ and $HPDP_\theta^{pq}$ are the PDP's histogram vectors extracted in the radial and the angular directions in the (p,q)th patch, respectively.

For measure the dissimilarity between the query image and the model, two distance vectors are computed. The first distance vector is Polar Gabor Topography Distance Vector (PGTDV) which demonstrates the difference between the two patches in the query topography map f and the model topography map g:

$$
PGTDV^{pq} = \{[PGTV^{pq}]_f - [PGTV^{pq}]_g\}
\tag{28}
$$

The second distance vector is Polar Derivative Distance Vector (PDDV) which shows the distance between the patches in the query texture map f and the model texture map g:

$$
PDDV^{pq} = \{[HPDP^{pq}]_f - [HPDP^{pq}]_g\}
\tag{29}
$$

By using $PGTDV^{pq}$, and $PDDV^{pq}$, we can compute dissimilarity (D) between the query image and the model as

$$
D = ((1-w_b).(\sum_{p=1}^{\lfloor r_{\max}/w_r \rfloor} \sum_{q=1}^{\lfloor 2\pi/w_\theta \rfloor} \|PDDV^{pq}\|^2) + (w_b).(\sum_{p=1}^{\lfloor r_{\max}/w_r \rfloor} \sum_{q=1}^{\lfloor 2\pi/w_\theta \rfloor} \|PGTDV^{pq}\|^2))^{1/2}
\tag{30}
$$

where the symbol $\|\cdot\|$ represents the Euclidean norm of the vector and w_b is a balancing weight determined experimentally.

3   Experimental Results

The robustness of the proposed algorithm in the face recognition task under the pose rotation and the expression variation is investigated. In our experiments, the Bosphorus database [14] is used that contains faces with pose rotations and expression changes. In the experiments, preprocessing was applied to face scans in the database. Spikes in 3D faces were removed using median filtering in the z-coordinate. Holes were filled using cubic interpolation and 3D scans were resampled on a uniform square grid at 1 mm resolution. Finally, all scans were subjected to pose normalization and cropped to the size of 120×120 pixels.

The Bosphorus database [14] contains 105 subjects (61 females and 44 males) with a total of 4666 faces. The images include frontal views with different facial expressions, pose variations, and occlusions. The resolution in x, y, and z (height) dimensions are 0.3 mm, 0.3 mm, and 0.4 mm respectively, and color texture images are high resolution (1600×1200 pixels). To compute the accuracy of the proposed method, we consider faces with expression and pose variations in the database (see Fig. 2). The robustness against the pose rotation is one of the most major problems in the accuracy computing of the face recognition systems. Here, we evaluate the acceptable performance of the proposed method using faces with pose variations from the Bosphorus database [14]. There are 11 different poses including left 45°, right 10°, right 20°, right 30°, right 45°, right down, right up, slightly up, strong up, slightly down, and strong down for each subject. Since our goal is to solve the problem of the face recognition using one exemplar per person case, as the gallery, one frontal image per enrolled subject is used.

The rank-1 recognition rate of the our approach is shown in Table 1. We compare proposed method with the recognition rates of the methods in [8] and [10] as the benchmarks. For faces with small yaw rotations (right 10°, right 20°, and right 30°), the rank-1 recognition rate is higher than 98%, while it is higher than 91% for faces with large yaw rotations (right 45° and left 45°). In upward pitch rotations, our method achieves 100% recognition rate for small and

Fig. 2. Images of a subject in the Bosphorus database [14] with different poses and expressions.

Table 1. Comparison the rank-1 recognition rates of the proposed method and the benchmarks under the pose variations.

Considered rotation	Proposed method	Hajati et al. [8]	Malassiotis and Strintzis method [10]
Right 10°	100	92.3	65.7
Right 20°	100	88.6	52.4
Right 30°	98.1	80	42.9
Right 45°	91.4	39	9.5
Left 45°	91.4	38.1	21
Up (Slight)	100	87.6	81.9
Up (Strong)	100	79	69.5
Down (Slight)	99.1	87.6	84.8
Down (Strong)	97.1	69.5	68.6
Right-Up	94.3	63.8	31.4
Right-Down	90.5	34.3	21.9
Average	**96.5**	**69.1**	**50**

strong rotations, while the benchmarks have 87.6% and 81.9% for small rotations and 79% and 69.5% for strong rotations, respectively. For downward pitch rotations, the accuracy rate of the proposed method is 99.1% and 97.1% in small and strong rotations, respectively. The rank-1 recognition rate of the proposed method is 94.3% and 90.5% for faces with the right-upward rotation and the right-downward rotation, respectively. Overall, the proposed method achieves the average recognition rate of 96.5% across all rotations in the database, outperforming [8] and [10] with 69.1% and 50%, respectively.

We also evaluate the performance of the proposed method under the expression changes using the Bosphorus database [14]. For this purpose, we report the rank-1 recognition rate of the proposed method using all faces with pose and

Table 2. Comparison the rank-1 recognition rates of the proposed method and the benchmarks under the expression variations.

Method	Recog. Rate	Gallery	Probe
Baseline ICP [15]	72.4%	47 (Frontals)	1508 (Expressions)
Baseline PCA [15]	70.6%	47 (Frontals)	1508 (Expressions)
Alyüz et al. [16]	95.3%	47 (Frontals)	1508 (Expressions)
Dibeklioğlu et al. [17]	89.2%	47 (Frontals)	1527 (Expressions)
Hajati et al. [8]	69.1%	105 (Frontals)	1155 (Expressions)
Proposed Method	**96.6%**	**105 (Frontals)**	**3696 (Expressions + Rotations)**

expression variations as the probe (see Table 2). The rank-1 recognition rate for the proposed method is 96.6% using 105 galleries and 3696 probes, while the best one among the benchmarks is 95.3% using 47 galleries and 1508 probes.

4   Conclusion

In this paper, a new approach called Polar Topographic Derivatives (PTD) was proposed for 3D face recognition. The PTD used both the range and the texture maps to extract discriminative features. We applied the PTD to expression and pose invariant face recognition purpose, and achieved considerable improvements in the recognition rates compared to the state-of-the-art methods. The experimental results demonstrate that the algorithm has an acceptable performance even though in large database. Although the proposed algorithm have been applied to 3D face recognition task, it can be generalized to other textured 3D shapes.

References

1. Hajati, F., Tavakolian, M., Gheisari, S., Gao, Y., Mian, A.S.: Dynamic texture comparison using derivative sparse representation: application to video-based face recognition. IEEE Trans. Hum.-Mach. Syst. **47**(6), 970–982 (2017)
2. Hajati, F., Cheraghian, A., Gheisari, S., Gao, Y., Mian, A.S.: Surface geodesic pattern for 3D deformable texture matching. Pattern Recognit. **62**, 21–32 (2017)
3. Abate, A.F., Nappi, M., Riccio, D., Sabatino, G.: 2d and 3d face recognition: a survey. Pattern Recognit. Lett. **28**(14), 1885–1906 (2007)
4. Chang, K.I., Bowyer, K.W., Flynn, P.J.: Face recognition using 2d and 3d facial data. In: ACM Workshop on Multimodal User Authentication, pp. 25–32 (2003)
5. Bowyer, K.W., Chang, K., Flynn, P.: A survey of approaches and challenges in 3d and multi-modal 3d + 2d face recognition. Comput. Vis. Image Underst. **101**(1), 1–15 (2006)
6. Smeets, D., Keustermans, J., Vandermeulen, D., Suetens, P.: meshsift: Local surface features for 3d face recognition under expression variations and partial data. Comput. Vis. Image Underst. **117**(2), 158–169 (2013)
7. Alyuz, N., Gokberk, B., Akarun, L.: Regional registration for expression resistant 3-d face recognition. IEEE Trans Forensics Secur. **5**(3), 425–440 (2010)
8. Hajati, F., Raie, A.A., Gao, Y.: 2.5d face recognition using patch geodesic moments. Pattern Recognit. **45**(3), 969–982 (2012)
9. Lee, T.: Image representation using 2d gabor wavelets. IEEE Trans Pattern Anal. Mach. Intell. **18**(10), 959–971 (1996)
10. Malassiotis, S., Strintzis, M.G.: Robust face recognition using 2d and 3d data: pose and illumination compensation. Pattern Recognit. **38**(12), 2537–2548 (2005)
11. Bronstein, A.M., Bronstein, M.M., Kimmel, R.: Three-dimensional face recognition. Int. J. Comput. Vis. **64**(1), 5–30 (2005)
12. Mian, A.S., Bennamoun, M., Owens, R.: An efficient multimodal 2d–3d hybrid approach to automatic face recognition. IEEE Trans. Pattern Anal. Mach. Intell. **29**(11), 1927–1943 (2007)

13. Zhang, H., Gao, W., Chen, X., Zhao, D.: Learning informative features for spatial histogram-based object detection. In: Proceedings of the International Conference on Neural Networks, vol. 3, pp. 1806–1811 (2005)
14. Savran, A., Alyüz, N., Dibeklioğlu, H., Çeliktutan, O., Gökberk, B., Sankur, B., Akarun, L.: Biometrics and identity management. Bosphorus Database for 3D Face Analysis, pp. 47–56 (2008)
15. Alyüz, N., Gökberk, B., Dibeklioğlu, H., Savran, A., Salah, A., Akarun, L., Sankur, B.: Biometrics and identity management. In: Biometrics and Identity Management, pp. 57–66. Springer, Heidelberg (2008)
16. Alyüz, N., Gökberk, B., Akarun, L.: A 3d face recognition system for expression and occlusion invariance. In: Proceedings of the IEEE Second International Conference on Biometrics Theory, Applications and Systems, pp. 1–7 (2008)
17. Dibeklioğlu, H., Gökberk, B., Akarun, L.: Nasal region-based 3d face recognition under pose and expression variations. In: Proceedings of the Third International Conference on Advances in Biometrics, vol. 5558, pp. 309–318 (2009)